Bernardo João Ribeiro Simões

Licensed in Materials Engineering

Microstructure and Mechanical properties in Cu-17Al-11.4Mn shape memory alloys laser welded to 316L stainless steel

Dissertation to obtain the Master's Degree in

Materials Engineering

Supervisor: Prof. Doutor João Pedro Oliveira, Invited Assistant Professor, DEMI FCT NOVA

Jury

President: Dr. Rui Jorge Cordeiro Silva, Associate Professor, DCM FCT NOVA

Rapporteur: Dr. Rui Fernando dos Santos Pereira Martins, Associate Professor, DEMI FCT NOVA

Member: Dr. João Pedro de Sousa Oliveira, Invited Assistant Professor, DEMI FCT NOVA

FACULDADE DE CIÊNCIAS E TECNOLOGIA
UNIVERSIDADE NOVA DE LISBOA

Microtructure and Mechanical Properties in Cu-17Al-11.4Mn shape memory alloys laser welded to stainless steel

To my parents…

Acknowledgements

To my supervisor, for giving me the opportunity to work on a subject I love to explore, all the guidance and constant support throughout this work and motivating me to do my best.

To Mr. Amirali Shamsolhodaei, from the University of Waterloo, Canada, for all the help given even an ocean away during these different and hard times.

To my colleagues Beatriz and Lourenço, who shared the same supervisor with me. Thank you for all the support and good times we shared in this journey of ours.

To my Academic friends, Rita, Pedro, Andreia, João, Madalena and Inês, for all the companionship, support and advice given.

Also, to my friends back home, Daniela, Tiago, Bruno and Daniel, for all the support for nearly twenty years and for their patience these last few months when I couldn't join them due to my work.

To my parents, for all their effort, support, love and confidence they gave me all my life and specially this last year. Without you, none of this would have been possible.

Lastly, I want to thank everyone whom I shared this journey with. Even though you were not named directly, know that I'm grateful for every single one of you and carry you all with me for the rest of my life.

Abstract

It is well known that NiTi alloys are the most widely used shape memory alloys nowadays, with a large number of possible applications, such as in the aerospace, automotive, medical and civil industries. This large versatility makes them a very difficult alloy to replace.

However, there is a group of shape memory alloys which has been receiving evermore attention as a candidate to replace NiTi alloys, with many of the same applications. These are the Cu-Al-Mn alloys, a lightweight group of alloys recognized for their large versatility and lower cost, while managing to achieve the same or even better results than NiTi in certain scenarios, specially the Cu-17Al-11.4Mn (at. %) alloy. However, little is known about how this alloy's properties behave when welded to other materials, which leaves a lack of knowledge regarding this alloy's versatility on this issue.

In this dissertation, this alloy laser welded to stainless steel to study the welding process's effects on it together with the influence of the 316L low carbon stainless steel it is welded to. For this effect, the welded alloy was subjected to microstructural and mechanical testing, such as Scanning Electron Microscopy, Electron Backscatter Diffraction, Energy-Dispersive X-ray Spectroscopy and X-ray Diffraction, as well as Microhardness Mapping, Mechan-ical Cycling and Uniaxile Tensile Testing. This study shows that the welding process heavily influences the microstructural composition of the fusion zone, such as grain size and orientation while, on a mechanical level, also reinforcing the alloy's superelastic properties together with the steel.

Keywords: Shape memory alloys, Superelasticity, Laser welding, Cu-Al alloys, CuAlMn,

Resumo

É sabido que as ligas NiTi são as ligas de memória de forma mais amplamente utilizadas atualmente, com o seu grande número de possíveis aplicações, como é o caso nas indústrias aeroespacial, automóvel, médica e civil. Esta grande versatilidade torna estas ligas bastante difíceis de substituir.

No entanto, existe um grupo de ligas de memória de forma que tem recebido cada vez mais atenção como candidato a substituir as ligas NiTi, com muitas das mesmas aplicações. Estas são as ligas Cu-Al-Mn, um grupo de ligas leves reconhecidas pela sua grande versatilidade e custo reduzido, capazes de atingir os mesmos ou até melhores resultados do que NiTi em certos cenários, especialmente a liga Cu-17Al-11.4Mn (at. %). No entanto, pouco se sabe sobre como as propriedades desta liga se comportam quando soldadas a outros materiais, deixando uma falta de conhecimento sobre a versatilidade desta liga neste assunto.

Nesta dissertação, esta liga foi soldada a laser a um outro material, aço inoxidável, para estudar os efeitos do processo de soldadura nela juntamente com a influência do aço inoxidável ao qual se encontra soldada. Para este efeito, a liga soldada foi sujeita a ensaios microestruturais e mecânicos, como Microscopia Eletrónica de Varrimento, Difração de Eletrodispersão Eletrónica, Espectroscopia de Energia Dispersiva e Difração de raios X, bem como Mapeamento de Microdurezas, ensaios de Ciclagem Mecânica e de Tensão Uniaxial. Este estudo mostra como o processo de soldadura influencia fortemente a composição microestrutural da zona de fusão, como o tamanho de grão e sua orientação enquanto, mecanicamente, também reforça as propriedades superelásticas da liga juntamente com o aço.

Keywords: Ligas com memória de forma, Superelasticidade, Soldadura laser Nd:YAG, Ligas Cu-Al, CuAlMn

Índice Geral

Table of Tables

Table of Figures

Table of Abbreviations

A_s	Austenite transformation start temperature
BM	Base Material
EBSD	Electron Backscatter Diffraction
EDS	Energy-Dispersive X-ray Spectroscopy
FZ	Fusion Zone
HAZ	Heat Affected Zone
M_f	Martensite transformation finish temperature
M_s	Martensite transformation start temperature
SE	Superelasticity
SEM	Scanning Electron Microscopy
SMA	Shape Memory Alloys
SME	Shape Memory Effect
SS	Stainless-steel
XRD	X-ray Diffraction

1 Introduction

1.1 Motivations

It is well known that the most used shape memory alloy, with various possible applications, is NiTi. Cu-Al band alloys, specially CuAlMn, present themselves as good substitutes with many of the same applications [1–3]. However, little is known about this alloy's relation with other materials and how welding them together can affect the shape memory and superelastic effects of the alloy.

There is also little knowledge about possible applications when welding this alloy to other metals. Therefore, facing this lack of knowledge around this subject, this study is justified by aiming to improve the knowledge on how the mechanical and microstructural properties of the SMA in question can be improved by welding it to another material, in this case, stainless steel.

1.2 Objectives

The main objective of this dissertation is to determine the effects of laser welding of CuAlMn to SS. To achieve this goal, several mechanical and microstructural tests were conducted on the joints.

1.3 Dissertation Structure

It was determined that this dissertation would be divided in 5 different chapters, with various subchapters except for the final one.

The first chapter, titled Introduction, presents the main goals of this dissertation as well as the motivations found that led to its development and this description of the dissertation's structure.

In the second chapter, designated Bibliographical Review, a review is made of all subjects related to the work involved deemed necessary to have a previously established knowledge of. This chapter begins with an explanation of how shape memory alloys work, with special attention given to the superelasticity and shape memory effects, respectively. Afterwards, an approach to Cu-Al-Mn alloys specifically is made, as well as a review on the process of laser welding.

The third chapter, named Materials and Methods, goes in depth on describing the manufacture process of the alloy specimens, as well as a description of all the experimental procedures executed for each of the tests performed.

The fourth chapter, titled Results and Discussion, presents and discusses the results originated from the tests performed mentioned in the previous chapter.

The fifth and final chapter contains all the conclusions resulting from the work performed as well as proposals for future projects.

2 Bibliographic Review

2.1 Shape memory alloys

Shape memory (SM) and superelasticity are two properties within some metallic alloys which have been getting ever more attention for their practical applications. Some metallic materials possess the ability to undergo a non-permanent plastic deformation, returning to their original shape when heated. When these alloys are deformed within a specific temperature range, they are also able of undergoing elongations of approximately 10%, and yet, are still able to return to their original physical shape when resting [1]. These phenomena are dubbed, respectively, Shape Memory Effect (SME) and Superelasticity (SE). Due to these properties, Shape Memory Alloys (SMAs) have been the cause of interest from many industries such as automotive and aerospace [2].

2.1.1 Superelasticity

The Superelastic Effect (SE) occurs without any temperature change, using only the application of stresses in the alloy. This effect occurs at temperatures above A_f, where the austenitic phase is more thermodynamically stable, in relation to the martensitic phase. When a tension is applied to the alloy, it is possible to cause a transformation of austenite into martensite. This transformation can be reversed by releasing the alloy from the stress applied, in which the martensitic phase will revert back to the initial austenitic phase, and relatively high strains (about 8 to 10%) can be applied, thanks to this property [4].

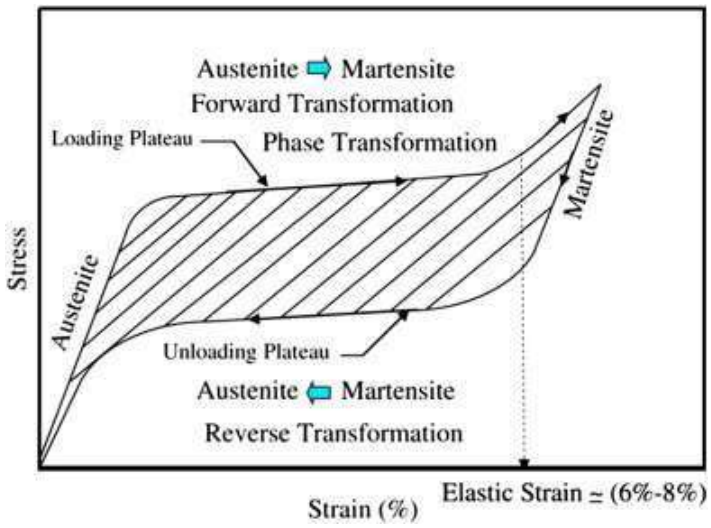

Figure 2.1 – Hysteresis of the superelasticity effect [4]

The alloys with superelasticity present high hysteresis, since the inverse transformation, that is, from the martensitic to austenitic phase, occurs at different stresses during unloading in relation to the stresses applied in the load associated with the first transformation, something that is also verifiable in thermal cycling tests, since it occurs due to the same reasons [5].

2.1.2 Shape memory effect

The Shape Memory Effect consists of the ability of the material to return to its initial structure after undergoing an apparent plastic deformation, by heating it. This effect arises because of a transformation of the crystalline phase of the metal at a certain temperature. Below the transformation temperature, these metal alloys present twinned martensitic phase, a soft phase capable of being deformed by detwinning. By heating these alloys to temperatures above the processing temperature, the material resumes its initial structure, transitioning from the martensitic phase to the austenitic phase.

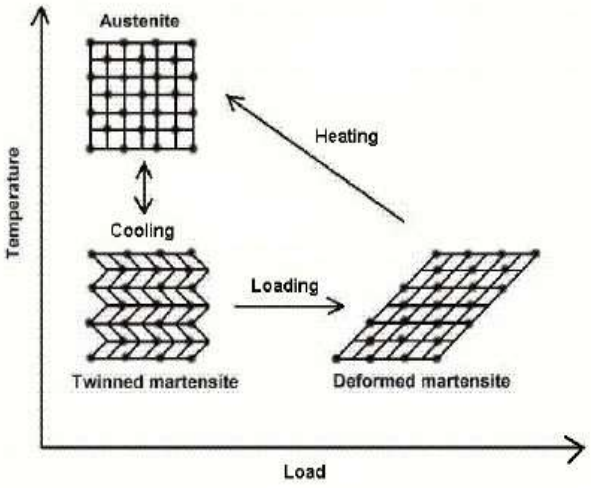

Figure 2.2 – phase transitions in shape memory alloys [6]

Hysteresis associated with heating and cooling of an SMA is a very important feature. The shape of the hysteresis curve of an alloy can vary greatly depending on the type of metal alloy used and/or how it was produced.

2.1.3 CuAlMn alloys

While NiTi-based alloys are currently still the most used shape memory alloys with various possible applications [7], Cu-based shape memory alloys have been receiving ever more attention as possible cheaper substitutes, making these two alloy types the most studied in their class [8] with virtually the same applications, with special attention beinggiven to seismic [3] and medical applications [1,2]

From the Cu-based SMAs, the Copper-Aluminium (Cu-Al) system is considered the most relevant and important one. However, the SM properties of the binary alloy itself are somewhat unstable. To correct this, the addition of a third element like Manganese (Mn) can greatly improve the alloy's SM properties by stabilizing its β phase [9].

The amount of Al present in the alloy's composition also holds significant importance to how they behave and perform. Cu-Al alloys show better ductility with low amounts of Al, preferably lower than 18 at. % [9]. Therefore, in this study, a Cu-17Al-11.4Mn (at. %) alloy will be analysed.

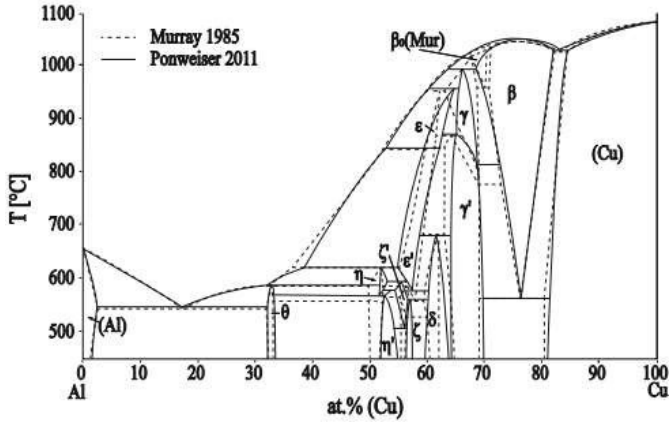

Figure 2.3 – The Cu-Al phase diagram[10]

2.2 Laser welding

Laser *(light amplification by stimulated emission of radiation)* has proved itself very useful in several areas. In a laser there is emission of stimulated light: a photon collides with an excited atom, leading to the emission of a photon with the same properties. However, the input photon must contain the energy required for this process to occur.

After the stimulated emission, the new photon has the same frequency, position and direction as the first phase of the photon. The increase in the number of photons will provide an amplification phenomenon: the light beam will also increase. Whenever a photon collides with the excited atoms, they can generate more photons and in this way the ray of light will increase again. This phenomenon allows us to understand why lasers are also known as light amplifiers [11].

During the incidence of a laser beam, beam radiation, when interacting with matter, is part absorbed and part reflected, thus occurring welding.

Absorbed radiation heats the material leading to melting or vaporization depending on energy density. In keyhole welding the beam has enough intensity to cause evaporation in the center of the melting bath. This leads to the so-called *keyhole,* a channel formed by steam and plasma (of the protective gas and the metal) which increases the ratio between the width and depth of the weld [12]. As the process is dynamic, the displacement of the part will guarantee the support of the *keyhole.* With the displacement of the *keyhole,* the mass of liquid material will solidify, thus occurring welding [13]. This

welding mode is widely used when it is necessary to reach greater penetration depths [12].

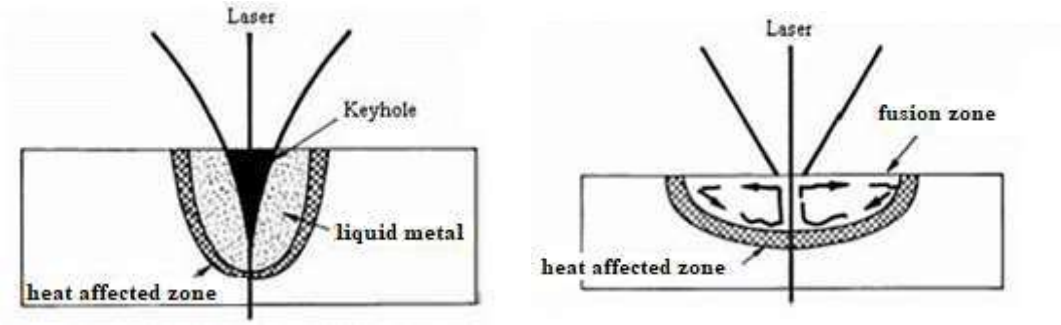

Figure 2.4 – Keywhole welding (left) and conduction welding (right) [12]

In case the energy is not sufficient for vaporization (and is for fusion only), conduction welding will occur, which will have a mechanism extremely similar to conventional welding processes, with heat dissipated laterally [13]. That is, in conduction welding, the material is heated until it fuses, and the laser energy is not enough to evaporate the material.

2.2.1 Dissimilar Welding

Joining dissimilar materials together is a common occurrence in complex industrial applications, like those seen in the automotive and aeronautical industries [14]. However, the process of joining together two metals with different properties, such as an SMA and a stainless steel is a complicated process [15].

Laser welding is one of the most used methods of joining dissimilar metals, with its rapid heating/cooling gradients, high precision and very local heat supply [16]. This is a similar process as that of welding to similar metals together, with a laser beam focused on the metals until a joint connection is formed, but special attention must be given to factors such as solubility, weldability, corrosion and possible intermetallic compounds formed within the transition zone [14,17].

Dissimilar laser welding, however, makes it possible to further expand a material's applications by joining it to another, especially in the medical, aerospace and automotive industries, with great interest being given in exploring new smart structures for these industries [17].

3 Materials and Methods

3.1 Materials

There were two types of samples that were used throughout the experimental procedures. These samples were comprised of unwelded base material (BM) and of base material laser welded to stainless steel (SS).

The SS used consists of 316L stainless steel wire by McMaster-Carr. This is a kind of austenitic stainless steel commonly used for industrial equipment, such as piping and super-heated tube material exposed to high temperatures [18,19].

As previously stated, the base material consists of a Copper, Aluminium and Manganese alloy (CuAlMn). The Cu-17Al-11.4Mn (at. %) ingots were prepared through the use of induction melting under an Argon atmosphere. The ingots were then hot forged and cold drawn in order to produce wires with diameters of 0,5 mm. To obtain large enough grains [20], these wires were repeatedly annealed at 900ºC. After a solution heat treatment at 900ºC, they were then water quenched and aged at 200ºC to stabilize the martensitic structure.

These heat treatments formed an oxide layer on the wires, which was removed using fine SiC paper, resulting in a final diameter of the wires of 0.485±0,005mm. The wires were then cleaned with acetone and ethanol to avoid any impurities that might be detrimental to the laser welding process.

3.2 Methods

3.2.1 Laser Welding

For the laser weld process, a pulsed Nd:YAG laser system from Miyachi Unitek LW50A to perform bead-on-plate welds with a 1064 nm wavelength, a top-hat type spatial profile and a spot size of 600 µm was used with Argon used as gas shielding at a flow rate of 0.57 m^3h^{-1}. The pulse had a profile with a duration of 6 ms, including 1 ms upslope and 1 m downslope. This welding process was developed to achieve full penetration with a symmetric contour and minimum heat input. Butt joint welds were performed with a peak power of 1.5 kW.

3.2.2 Microstructural characterization

For metallographic analysis after welding, the samples were prepared by mechanical polishing and etching.

To understand more thoroughly the microstructural evolution of the welded samples, a Zeiss Ultra Plus field emission scanning electron microscope (SEM) equipped with Energy dispersive spectroscopy (EDS) was used. EDS was also used to better assess the homogeneity of the welds' fusion zone and heat affected zone chemical compositions.

Electron Back-Scattered Diffraction (EBSD) was used to determine existing phases and crystallographic orientation throughout the welded joints.

For the identification of the phases present at room temperature, as well as their characterization, X-ray diffraction (XRD) was performed on a single sample through the use of a *Brucker* difractometer with conventional Θ/2Θ scanning.

Finally, with the purpose of identifying softening or hardening effects promoted by the welding process, hardness measurements were performed on the weld cross section, using a *Mitutoyo HM-112* microhardness tester with a test load of 100g,applied for 12 seconds. The microhardness tests were performed using 700 points to pro- vide excellent resolution., with indentations distancing 50 paces. These measurements allowed the construction of a bidimensional (x, y) map to help evaluate the changes in microhardness across the fusion zone all the way to the non-affected base material.

3.2.3 Mechanical characterization

In this section, two different sample groups than those from the microstructural characterization were tested.

Uniaxial Tensile testing was also performed on the base and welded material at room temperature, using an *Autograph Shimadzu AG50kNG* machine with a displacement rate equal to that of the cycling tests. For these tests, one base material and two welded samples were used. The surface fractures from the samples were observed with the same Zeiss Ultra Plus SEM from the microstructural characterization.

To evaluate the functional fatigue of the samples, Mechanical cycling was used with the same machine. The procedure consisted of straining the material to 5% followed by unloading to a condition of zero-stress. This process was repeated to a total of 50 cycles for the BM sample and 100 cycles for the welded sample, with a displacement rate of 1 mm/min. This procedure allowed to determine the evolution of irrecoverable strain, absorbed energy and maximum stress with the number of cycles. One specimen of un-welded CuAlMn and another of welded material were tested for this process.

4 Results analysis and Discussion

4.1 Microstructural characterization

4.1.1 SEM/EBSD and EDS

The superelastic recovery of single crystal SMAs like CuAlMn is highly dependent on the grain orientation and loading direction [21][22]. Therefore, with the purpose of properly analyzing the microstructure of the welded joint, hereby named Joint 1, was used for this effort. Figure 4.1 belongs to Joint 1. Also, for reference, the BM on the left of the figures is stainless-steel and the BM on the right is the CuAlMn alloy.

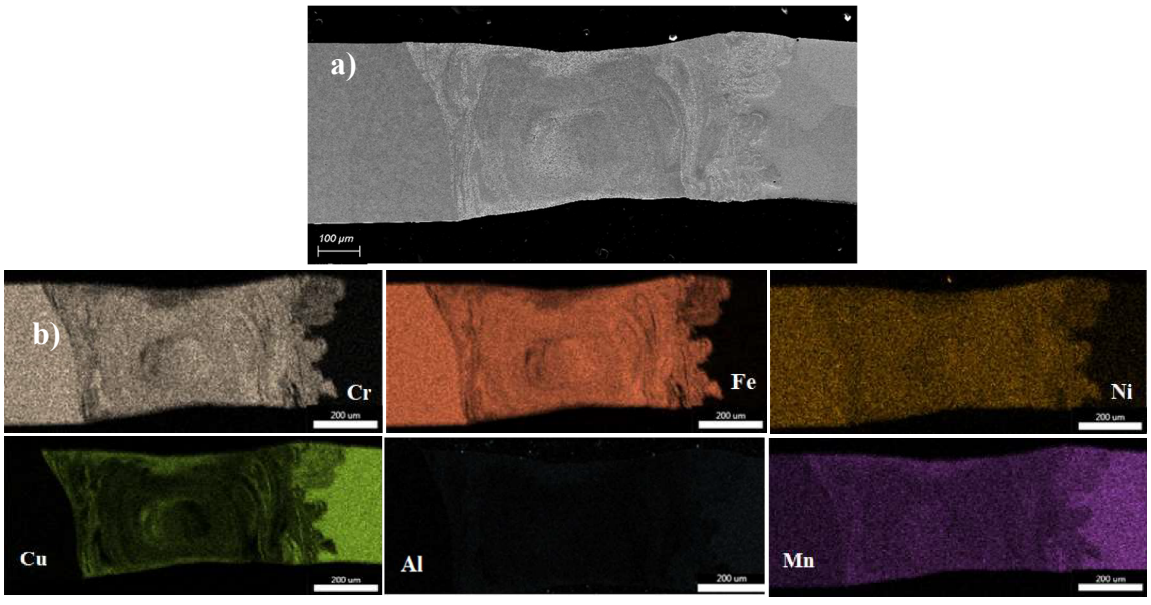

Figure 4.1 – a) SEM image of Joint 1; b) EDS images of Joint 1

Through the SEM image of Joint 1, the FZ and both BMs are very distinguishable from one another, with clearly different microstructures. There is no HAZ present in the

joint due to the pre-welding treatment performed on the BM [23–25]. The FZ itself showsno defects, and a full penetration joint was observed. There seems to be, however, a few islands and peninsulas of unwelded BM within the FZ and near the borders between the FZ and BM, as previously found in other dissimilar joints involving the CuAlMn shape memory alloy [1]

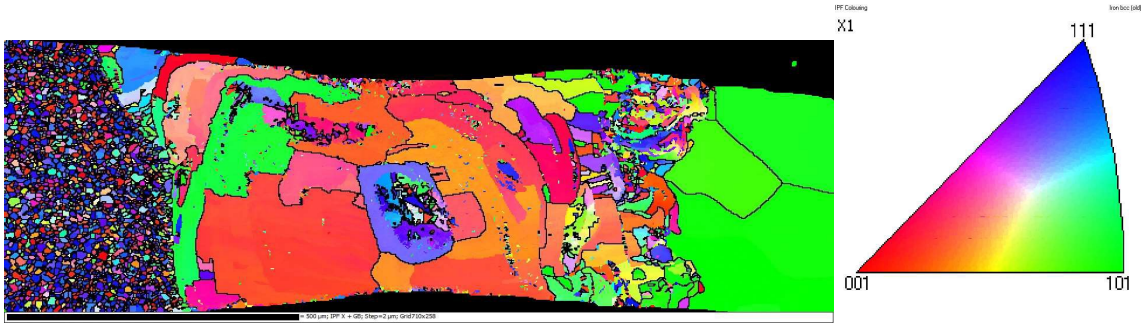

Figure 4.2 – EBSD image of Joint 1

EBSD imaging shows that Joint 1 has a very visible microstructural difference between the BMs and the FZ. The first thing of note is that the grains in the CuAlMn BM are very large and coarse with a preferential orientation towards the (101) direction whilst the stainless-steel grains appear to be very small with random orientations. In the FZ however, as we move away from the BM from either side, the grain structure seems to be changing from small, randomly oriented grains to large and coarse grains with preferred orientations around (001). These grains, however, are not growing together in a set direction, but in random directions which creates a non-ideal microstructure within the FZ [23]. Overall, while the base material consists of large coarse grains with a (101) orientation, the fusion zone consists of smaller, yet still coarse grains with a preferred (001) orientation, albeit with many smaller grains with randomized orientations also present. Images regarding transitional areas between both BMs and the FZ within Joint 1 can be found inAnnex A, for a clearer picture of the crystal orientations.

Finally, we can also notice that there are indeed two islands of unwelded base material from the stainless-steel within the FZ. These could be the result of parts of SS BMdislodging themselves during the welding process and moving inside the FZ to their finalposition.

EDS was also performed on Joint 1 to characterize the variations in composition along the weld, since the laser welding process can change a material's composition through vaporization [26]. On the borders between the BM and FZ, several regions were selected to measure its composition.

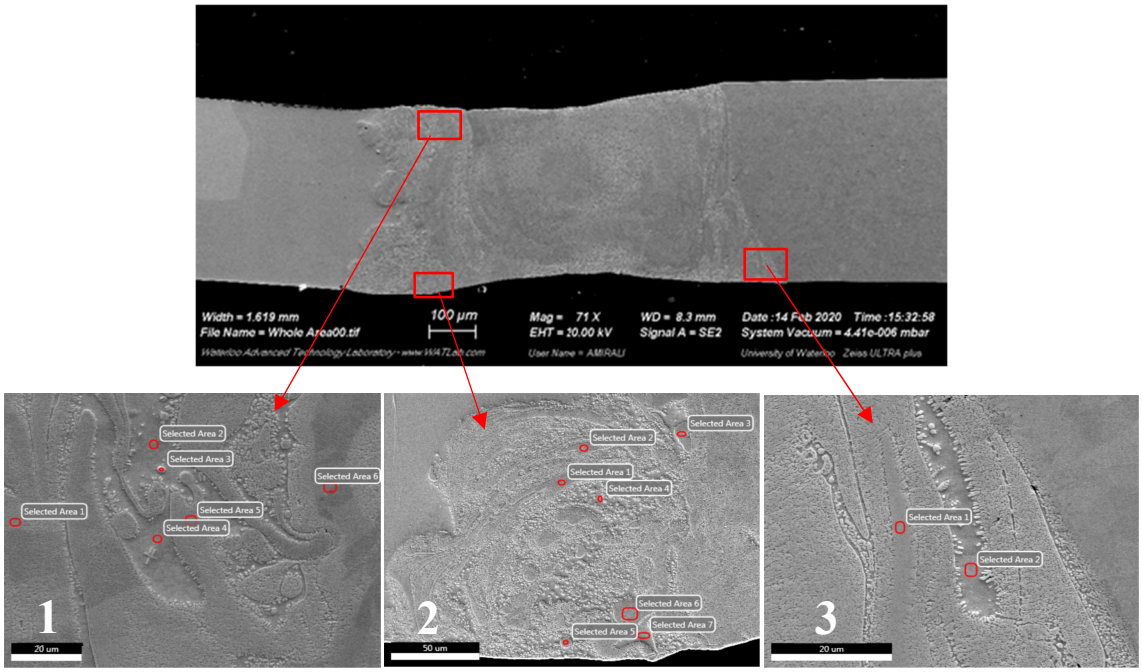

Figure 4.3 – Regions and areas selected for point analysis

Figure 4.3 shows the areas selected with a red circle for point analysis within three main areas, dubbed 1, 2 and 3, whose average values of atomic percentage are shown in *Table 4.1*. Through this data, it is possible to determine that the welding process caused no significant changes throughout the composition of the FZ, with iron and copper being the most prominent elements present, as expected.

	Average atomic Percentage (%)		
Elements	**Region 1**	**Region 2**	**Region 3**
Al	7,48	6,65	6,42
Cr	9,24	10,79	10,33
Mn	5,96	6,04	5,7
Fe	34,82	39,73	38,34
Ni	5,36	4,86	5,93
Cu	37,14	31,94	33,29

Table 4.1 - Average EDS measurements within selected regions of the FZ-BM border

4.1.2 XRD

As previously stated, XRD was performed identify and analyze the existing phases, with Joint 1 being the sample studied once again.

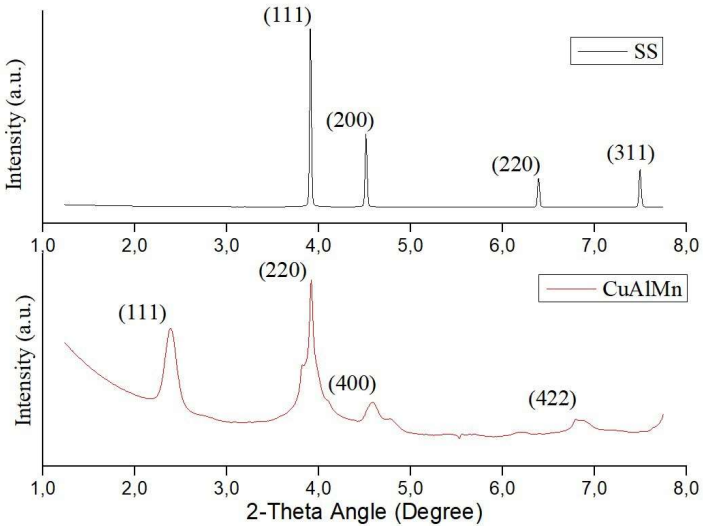

Figure 4.4 - Base material (SS and CuAlMn) diffractogram

On both BMs, results obtain show that there were no significant differences between the phases, since both BMs were fully composed of austenite.

4.1.3 Microhardness

Microhardness mapping was performed on the FZ area, from BM to BM. In *Figure 4.5*, a hardness mapping of the Joint 1 sample from before can be found with a representative trend of the hardness results found between the BMs (SS on the right and CuAlMn on the left).

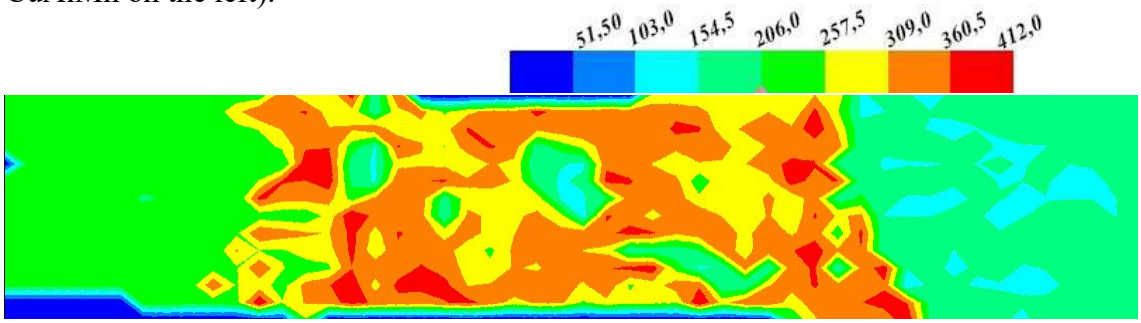

Figure 4.5 – microhardness mapping of Joint 1

The first thing to notice is the clear difference in hardness found in the fusion zone, which has much higher average values when compared to both BMs. This is related to the high iron content from the stainless-steel present inside the FZ that the EDS results previously presented [27].

There are also two large areas within the FZ that show hardness values on par with those of the SS BM, the same areas as showed in EBSD. Through the microhardness

mapping, these areas were identified as unmixed islands of SS-like composition. The same mapping shows there are also several unmixed peninsulas along the borders between the CuAlMn-BM and the FZ [1].

4.2 Mechanical characterization

4.2.1 Uniaxial Tensile Testing

As previously mentioned, three samples were used for this test, one unwelded and two welded, with the CuAlMn base material sample being used for reference. The figure below shows the curves resulting of this test.

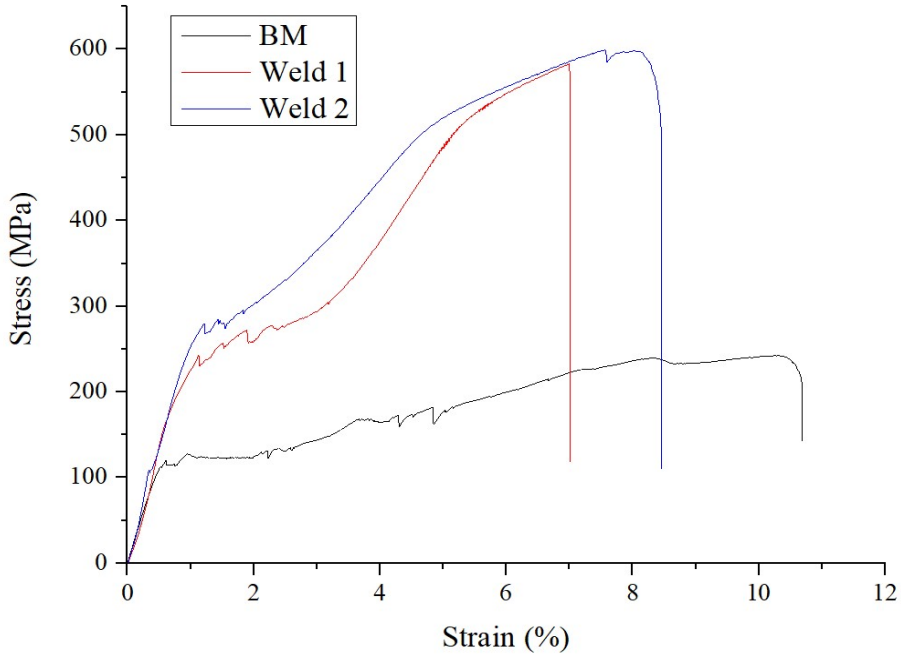

Figure 4.6 – Uniaxial tensile test curves for all three samples

While observing the curves, four distinct stages are distinguishable from eachother for all samples. The austenitic elastic deformation occurs right at the start, at an approximate 100 MPa for the base material and between 240 and 275 MPa for both welded joints. Next comes the transformation stage of austenite to twinned martensite, occurring between 100 and 130 MPa for the unwelded BM and roughly between 300 and 350 MPa for the welded joints. The third stage happens after all austenite is transformed to martensite, thus beginning the martensitic elastic deformation until if becomes fully detwinned, which appears to occur at 240 MPa for the unwelded material and all the way at 510 MPa

for the first welded joint and 520 MPa for the second one. At this point, the first weld suffers an immediate failure and fractures. Lastly, both remaining samples go through plastic deformation of the detwinned martensite. The BM sample is able to keep undergoing plastic deformation for longer than the welded joint, as the latter loses that ability. This happened due to a change in the orientation of the grains within the FZ, which lose their preferred orientation, making the joint also suffer mechanical failure sooner.

The BM sample was able to achieve a maximum stress value of 232 MPa with a 10,61% strain at the point of fracture. The welded joints, however, achieved a 584 and 600 MPa stress value with a 7,02% and 8,45% strain at fracture for the first and second welded joints, respectively. The massive values of maximum stress for the welded joints are thanks to the steel welded to the alloy, giving it a very big boost in mechanical resistance. However, the non ideal microstructure within the welded joint's FZ affected the strain that the welded joints were able to support before reaching critical failure.

Fracture of the joint occurred at its FZ. Therefore, the surface fractures were promptly analyzed though SEM.

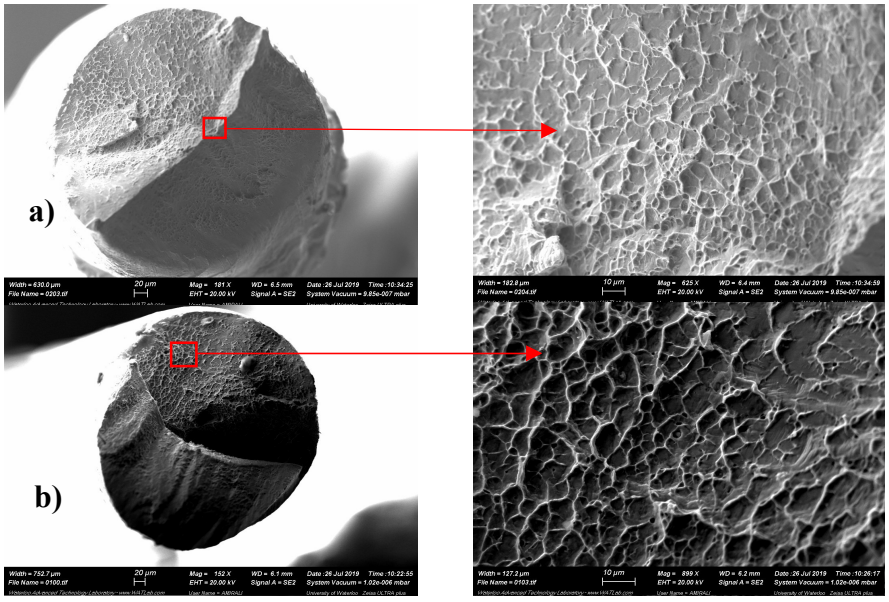

Figure 4.7 – a) surface fracture on SS side; b) surface fracture on BM side

Both sides of the fracture show numerous cavities, a characteristic of ductile fractures. During ductile fractures, microvoids are formed within the soon to be fracture surface, which cause these cavities [23,24,28]. More SEM images regarding surface fracture of the welded joint are available in Annex B.

4.2.2 Cyclic Tensile behavior

As previously mentioned in Materials and Methods, two samples were subjected to a cycling routine to evaluate their superelastic properties. To properly analyze the load-unload testing, the focus is mainly set on the maximum stress, irrecoverable strain and absorbed energy values when comparing both samples. The following graphs below show the main cycles of the tests performed on the unwelded CuAlMn BM and the same alloy welded to the stainless steel, respectively.

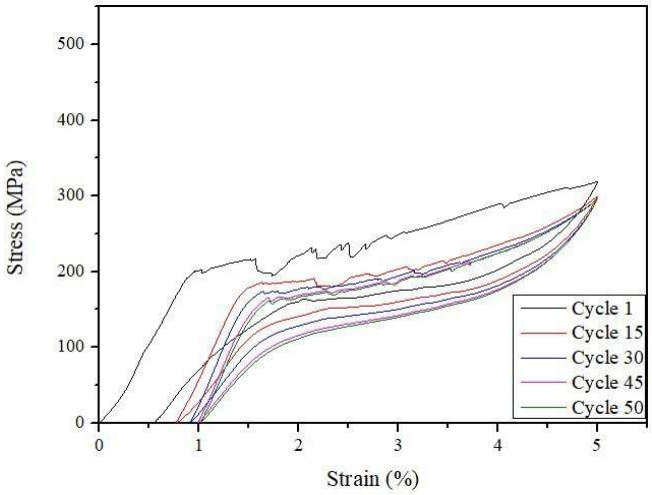

Figure 4.8 – Load-unload graph of main cycles of unwelded CuAlMn

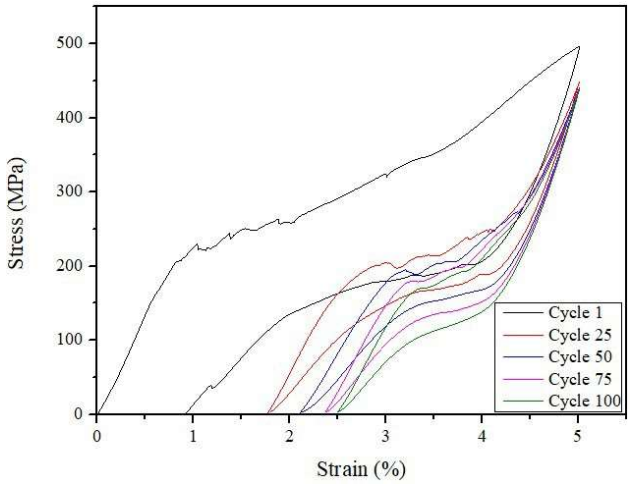

Figure 4.9 – Load-unload graph of main cycles of CuAlMn-SS joint

The first thing to notice is how clear the typical superelastic curve is in both the unwelded as in the welded samples, with the martensitic transformation happening at

roughly the same values. However, the first noticeable difference is in the maximum tension, where one can verify that the welded alloy manages to achieve much higher values than the unwelded CuAlMn, although at the cost of close to double the irrecoverable strain by cycle 50. The table below shows the exact values of this data for a clearer comparison. A higher irrecoverable strain from the welded joint is also noticeable. This is due to the unoptimized microstructure within the FZ as well as the presence of the SS, which suffered a plastic deformation.

	BM		Welded joint	
	Stress (MPa)	Strain (%)	Stress (MPa)	Strain (%)
Cycle 1	318,34	0,55	496,14	0,93
Cycle 50	296,56	1,02	440,16	2,12

Table 4.2 – Maximum tension and strain values for both samples' first and 50th cycle

4.2.3 Energy Absorbed

This joint's possible applications are highly dependent on its energy absorbing performance. The hysteresis of the welded joint in *Figure 4.6* shows the effect of the presence of stainless steel in the weld, with a noticeable degradation of the energy absorbed throughout the cycles, as is customary when subjecting steel to these tests [18,29,30].

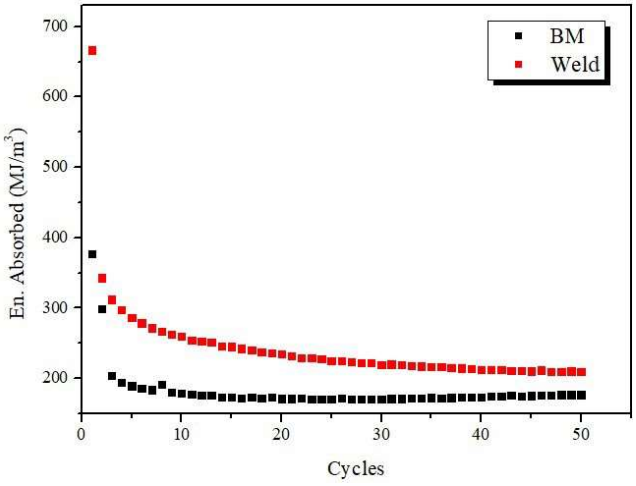

Figure 4.10 – Energy absorbed curbs for both unwelded (BM) and welded cycles

Both samples achieved a stabilized superelastic response after the first few cycles. The welded sample, however, was able to do so with higher levels of absorbed energy, due to the presence of the SS. However, the welded joint's energy absorption rate takes a

steeper fall during the first few cycles. This is due to the different microstructure properties between the BMs. Because stainless steel is not a superelastic alloy, it cannot achieve the same recovery as that of CuAlMn. Even so, these results indicate that the alloy and the steel may be considered together when planning and designing a structure, as the welded joint will not need to be subjected to a very high number of mechanical cycles before achieving its effective use during its application on said structure.

4.2.4 Irrecoverable Strain

As more and more cycles are performed on the weld, the irrecoverable strain tends to increase, due to occurring dislocation slips [31].

From *Table* 1, the irrecoverable strain for the unwelded sample after the first cycle is close to 0,5, well within expected values for this value [9]. On the welded sample, the larger value can be credited to the grains within the FZ, which although large, still possess a d/D ratio smaller than that of the unwelded alloy, together with the naturally small grains from the stainless steel, thus reducing the superelastic recovery after unloading [21].

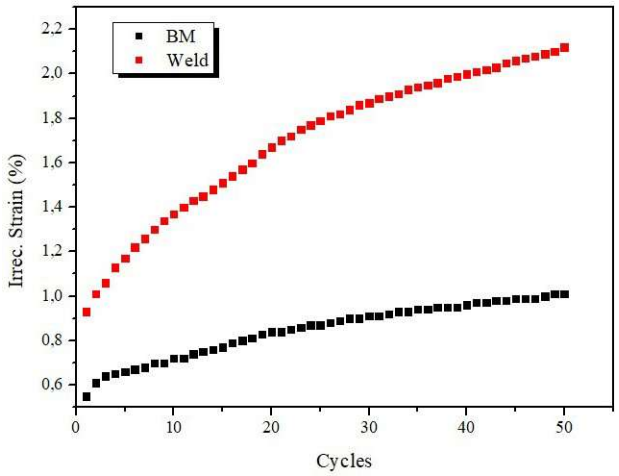

Figure 4.11 – Irrecoverable strain curves for both samples

4.2.5 Maximum Stress

As expected, the figure below shows how the accumulated defects on the material lead to a decrease in the maximum stresses they are able to support. Even so, the welded

material manages to behave better due in no small part to the steel's well-known capacity to achieve high values when under stress [18,29,30].

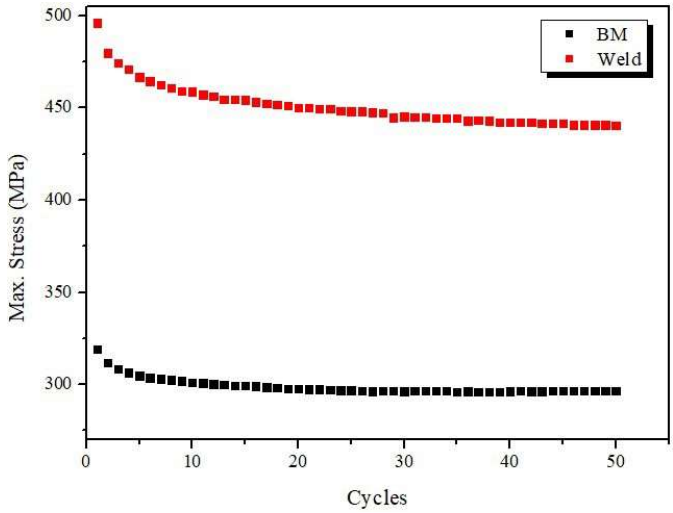

Figure 4.12 – Maximum stress curves for both samples

5 Conclusions and Future Perspectives

As previously mentioned, the main goal of this work was to study the effects of the laser weld on the Cu-17Al-11.4Mn (at. %) when welded to a different material, in this case, stainless steel, and how much it could affect the possible applications of this material. Therefore, samples of unwelded CuAlMn base material and CuAlMn-SS welded material were subjected to rigorous microstructural and mechanical testing, with the unwelded samples serving as a reference point.

The microstructural characterization consisted of SEM and EBSD imaging, with EDS, XRD and microhardness mapping being also performed. The results of this data showed that the laser weld had a clear influence in changing the grain size and orientation within the fusion zone. While the CuAlMn base material had very large grains oriented in the (101) direction, the fusion zone had mostly smaller, although still large, grains oriented in the (001) direction for Joint 1. The microhardness mapping also showed how the laser weld increased the general hardness of the grains within the fusion zone, when compared to both CuAlMn and SS.

The mechanical characterization consisted in uniaxial tensile testing with SEM fracture surface analysis and mechanical cycling testing. These tests showed that the superelastic effect of the base material is highly affected by the stainless steel's microstructural properties it is welded to. Tensile testing showed that the fusion zone microstructure affected the maximum strain supported by the welded joints, making it reach lower strain values than their unwelded counterpart. Mechanical cycling also showed how the hysteresis is affected by the FZ's microstructure, where the welded joint achieved higher maximum strain values throughout the cycles. However, the welded joint managed to reach higher levels of energy absorbed and showed itself capable of enduring much higher levels of maximum stress under the same conditions as the BM, which is of great interest for structural applications such as those seen in the aerospace and seismic industries while also giving opportunities for possible medical applications.

When it comes to future applications, these tests showed that it is of great interest to experiment with welding this alloy to other materials, as it shows to be incredibly versatile not only on its own but when joined to other materials, where it manages to combine both material's properties quite nicely. Therefore, more studies like this one should be performed with this alloy, under more extreme conditions to fully understand this alloy's limits when joined to other materials.

References

[1] J.P. Oliveira, Z. Zeng, C. Andrei, F.M. Braz Fernandes, R.M. Miranda, A.J. Ramirez, T. Omori, N. Zhou, Dissimilar laser welding of superelastic NiTi and CuAlMn shape memory alloys, Mater. Des. 128 (2017) 166–175. https://doi.org/10.1016/j.matdes.2017.05.011.

[2] R. Amini, S.M.M. Mousavizad, H. Abdollahpour, M. Ghaffari, M. Alizadeh, A.K. Okyay, Structural and microstructural phase evolution during mechano-synthesis of nanocrystalline/amorphous CuAlMn alloy powders, Adv. Powder Technol. 24 (2013) 1048–1053. https://doi.org/10.1016/j.apt.2013.03.005.

[3] H. Huang, Y.Z. Zhu, W.S. Chang, Comparison of Bending Fatigue of NiTi and CuAlMn Shape Memory Alloy Bars, Adv. Mater. Sci. Eng. 2020 (2020). https://doi.org/10.1155/2020/8024803.

[4] B. Asgarian, N. Salari, B. Saadati, Application of Intelligent Passive Devices Based on Shape Memory Alloys in Seismic Control of Structures, Structures. 5 (2016) 161–169. https://doi.org/10.1016/j.istruc.2015.10.013.

[5] H. Wang, P.D. Wu, J. Wang, Modeling inelastic behavior of magnesium alloys during cyclic loading-unloading, Int. J. Plast. 47 (2013) 49–64. https://doi.org/10.1016/j.ijplas.2013.01.007.

[6] J. Lim, Introduction to aerospace medicine, 2012. https://doi.org/10.5124/jkma.2012.55.7.649.

[7] J. Van Humbeeck, Non-medical applications of shape memory alloys, Mater. Sci. Eng. A. 273–275 (1999) 134–148.

[8] Y. Sutou, T. Omori, J.J. Wang, R. Kainuma, K. Ishida, Characteristics of Cu-Al-Mn-based shape memory alloys and their applications, Mater. Sci. Eng. A. 378 (2004) 278–282. https://doi.org/10.1016/j.msea.2003.12.048.

[9] R. Kainuma, S. Takahashi, K. Ishida, Thermoelastic martensite and shape memory effect in ductile Cu-Al-Mn alloys, Metall. Mater. Trans. A Phys. Metall. Mater. Sci. 27 (1996) 2187–2195. https://doi.org/10.1007/BF02651873.

[10] O. Zobac, A. Kroupa, A. Zemanova, K.W. Richter, Experimental Description of the Al-Cu Binary Phase Diagram, Metall. Mater. Trans. A Phys. Metall. Mater. Sci. 50 (2019) 3805–3815. https://doi.org/10.1007/s11661-019-05286-x.

[11] C. Furtado, Soldagem Laser, (2016).

[12] D. Ramos, W. De Rossi, J.R. Berreta, N. Dias, V. Jr, Soldagem a laser de ligas de titânio, (n.d.).

[13] A. Matsunawa, J.-D. Kim, N. Seto, M. Mizutani, S. Katayama, Dynamics of keyhole and molten pool in laser welding, J. Laser Appl. 10 (1998) 247–254. https://doi.org/10.2351/1.521858.

[14] M. Rossini, P.R. Spena, L. Cortese, P. Matteis, D. Firrao, Investigation on

dissimilar laser welding of advanced high strength steel sheets for the automotive industry, Mater. Sci. Eng. A. 628 (2015) 288–296. https://doi.org/10.1016/j.msea.2015.01.037.

[15] M.J. Torkamany, S. Tahamtan, J. Sabbaghzadeh, Dissimilar welding of carbon steel to 5754 aluminum alloy by Nd:YAG pulsed laser, Mater. Des. 31 (2010) 458–465. https://doi.org/10.1016/j.matdes.2009.05.046.

[16] I. Tomashchuk, D. Grevey, P. Sallamand, Dissimilar laser welding of AISI 316L stainless steel to Ti6-Al4-6V alloy via pure vanadium interlayer, Mater. Sci. Eng. A. 622 (2015) 37–45. https://doi.org/10.1016/j.msea.2014.10.084.

[17] M. Mehrpouya, A. Gisario, M. Barletta, S. Natali, F. Veniali, Dissimilar Laser Welding of NiTi Wires, Lasers Manuf. Mater. Process. 6 (2019) 99–112. https://doi.org/10.1007/s40516-019-00084-0.

[18] N. Moslemi, N. Redzuan, N. Ahmad, T.N. Hor, Effect of current on characteristic for 316 stainless steel welded joint including microstructure and mechanical properties, Procedia CIRP. 26 (2015) 560–564. https://doi.org/10.1016/j.procir.2015.01.010.

[19] M. Farid, P.A. Molian, High-brightness laser welding of thin-sheet 316 stainless steel, J. Mater. Sci. 35 (2000) 3817–3826. https://doi.org/10.1023/A:1004825213057.

[20] T. Omori, T. Kusama, S. Kawata, I. Ohnuma, Y. Sutou, Y. Araki, K. Ishida, R. Kainuma, Abnormal grain growth induced by cyclic heat treatment, Science (80-.). 341 (2013) 1500–1502. https://doi.org/10.1126/science.1238017.

[21] Y. Sutou, T. Omori, K. Yamauchi, N. Ono, R. Kainuma, K. Ishida, Effect of grain size and texture on pseudoelasticity in Cu-Al-Mn-based shape memory wire, Acta Mater. 53 (2005) 4121–4133. https://doi.org/10.1016/j.actamat.2005.05.013.

[22] J.L. Liu, H.Y. Huang, J.X. Xie, Superelastic anisotropy characteristics of columnar-grained Cu-Al-Mn shape memory alloys and its potential applications, Mater. Des. 85 (2015) 211–220. https://doi.org/10.1016/j.matdes.2015.06.114.

[23] J.P. Oliveira, B. Panton, Z. Zeng, T. Omori, Y. Zhou, R.M. Miranda, F.M. Braz Fernandes, Laser welded superelastic Cu-Al-Mn shape memory alloy wires, Mater. Des. 90 (2016) 122–128. https://doi.org/10.1016/j.matdes.2015.10.125.

[24] J.P. Oliveira, Z. Zeng, T. Omori, N. Zhou, R.M. Miranda, F.M.B. Fernandes, Improvement of damping properties in laser processed superelastic Cu-Al-Mn shape memory alloys, Mater. Des. 98 (2016) 280–284. https://doi.org/10.1016/j.matdes.2016.03.032.

[25] Y.T. Hsu, Y.R. Wang, S.K. Wu, C. Chen, Effect of CO2 laser welding on the shape-memory and corrosion characteristics of TiNi alloys, Metall. Mater. Trans. A Phys. Metall. Mater. Sci. 32 (2001) 569–576. https://doi.org/10.1007/s11661-001-0073-2.

[26] X.J. Yan, D.Z. Yang, Corrosion resistance of a laser spot-welded joint of NiTi wire in simulated human body fluids, J. Biomed. Mater. Res. - Part A. 77 (2006) 97–102. https://doi.org/10.1002/jbm.a.30378.

[27] S. Chen, J. Huang, J. Xia, X. Zhao, S. Lin, Influence of processing parameters on

the characteristics of stainless steel/copper laser welding, J. Mater. Process. Technol. 222 (2015) 43–51. https://doi.org/10.1016/j.jmatprotec.2015.03.003.

[28] P. Li, Q. Sun, L. Xiao, J. Sun, Tuning the morphology of Ti–5Al–5Mo–5V–3Cr–1Zr alloy: From brittle to ductile fracture, Mater. Sci. Eng. A. 769 (2020) 138487. https://doi.org/10.1016/j.msea.2019.138487.

[29] I. Tolosa, F. Garciandía, F. Zubiri, F. Zapirain, A. Esnaola, Study of mechanical properties of AISI 316 stainless steel processed by "selective laser melting", following different manufacturing strategies, Int. J. Adv. Manuf. Technol. 51 (2010) 639–647. https://doi.org/10.1007/s00170-010-2631-5.

[30] C. Jang, J. Lee, J. Sung Kim, T. Eun Jin, Mechanical property variation within Inconel 82/182 dissimilar metal weld between low alloy steel and 316 stainless steel, Int. J. Press. Vessel. Pip. 85 (2008) 635–646. https://doi.org/10.1016/j.ijpvp.2007.08.004.

[31] G. Eggeler, E. Hornbogen, A. Yawny, A. Heckmann, M. Wagner, Structural and functional fatigue of NiTi shape memory alloys, Mater. Sci. Eng. A. 378 (2004) 24–33. https://doi.org/10.1016/j.msea.2003.10.327.

Anexes

Anex A

CuAlMn- Stainless Steel

Joint 1 SS316/WZ Interface

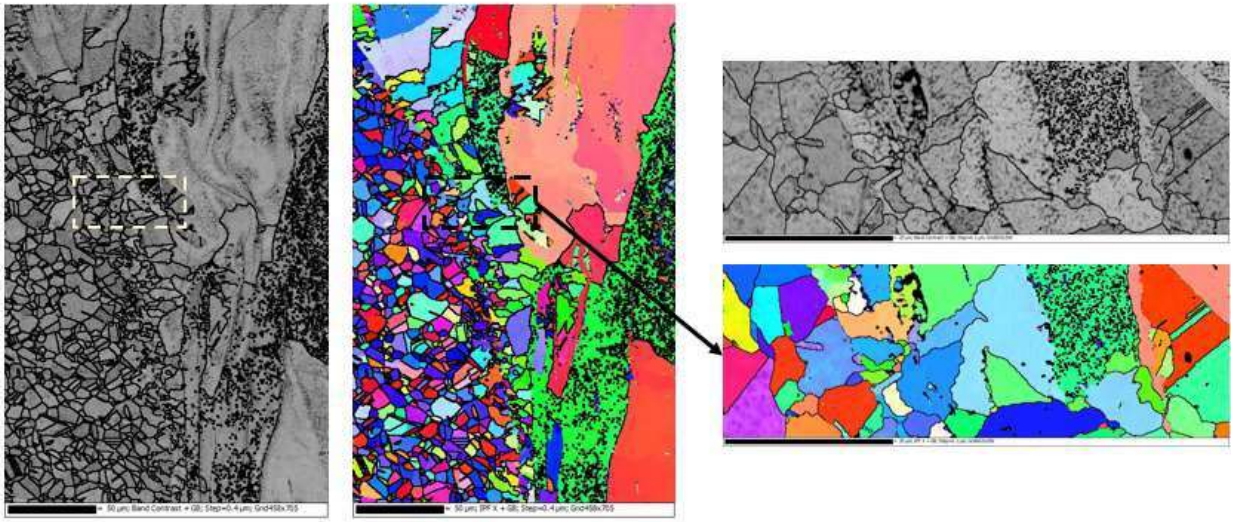

CuAlMn- Stainless Steel

Joint 1 CuAlMn/WZ Interface

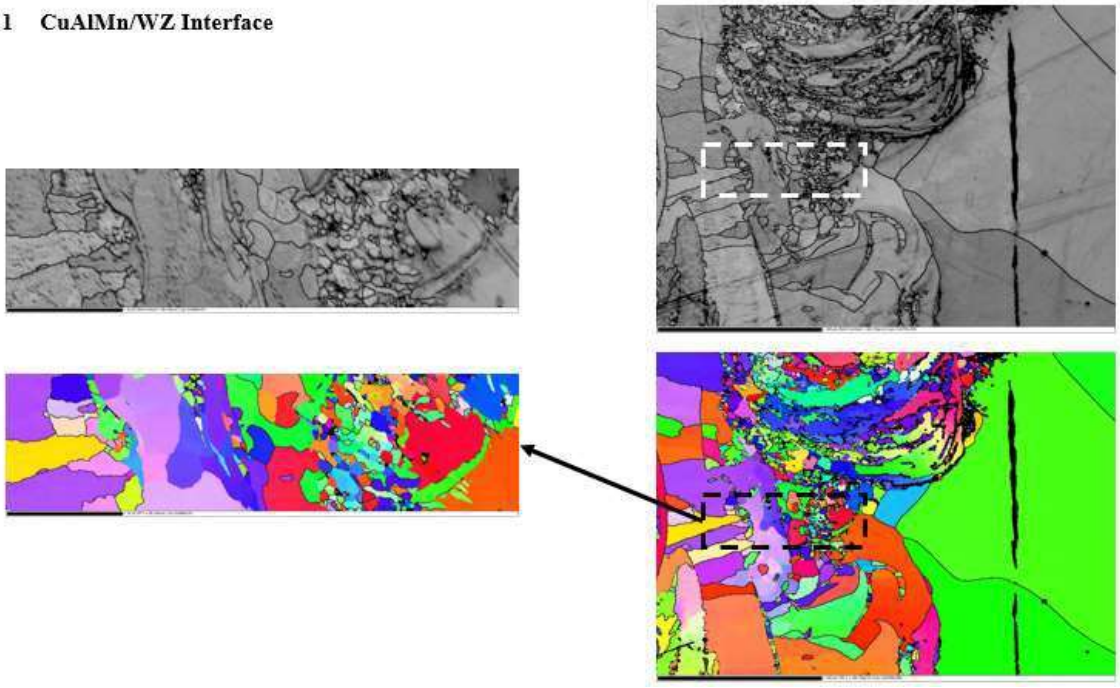

Anex B

316L Stainless Steel

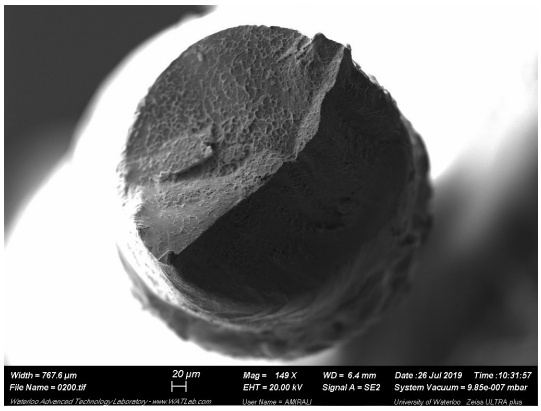

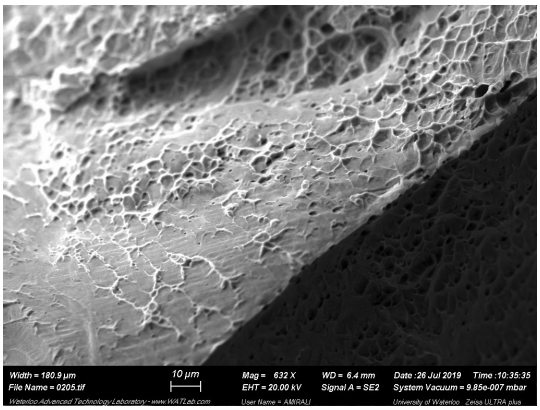

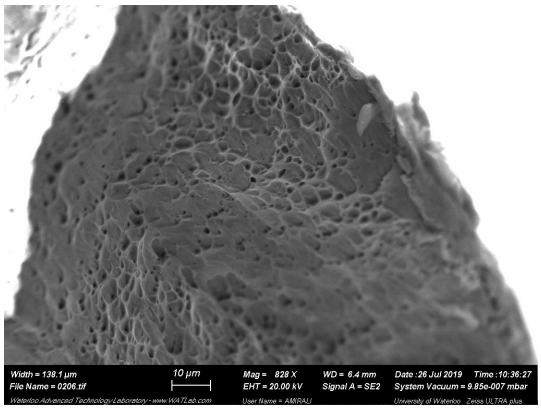

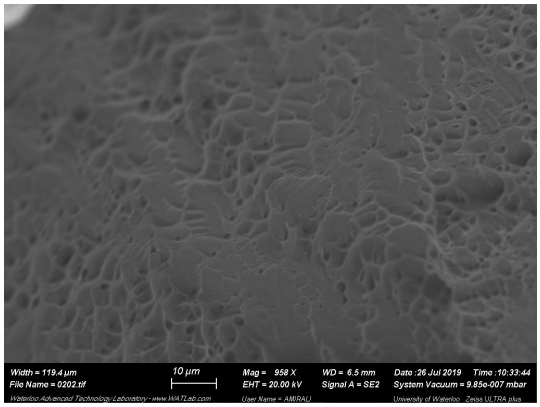

CuAlMn

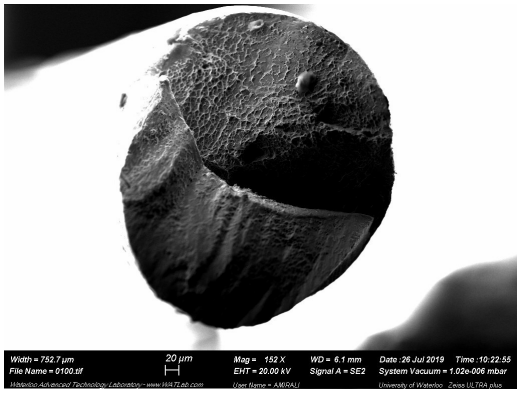

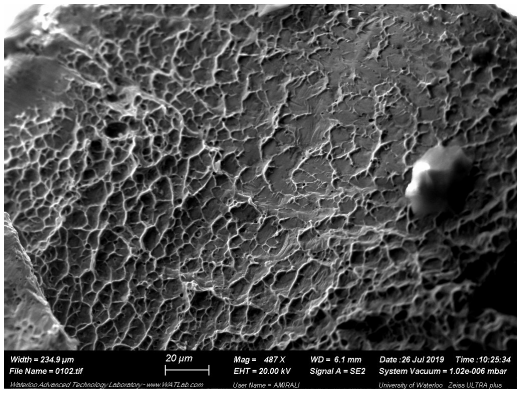

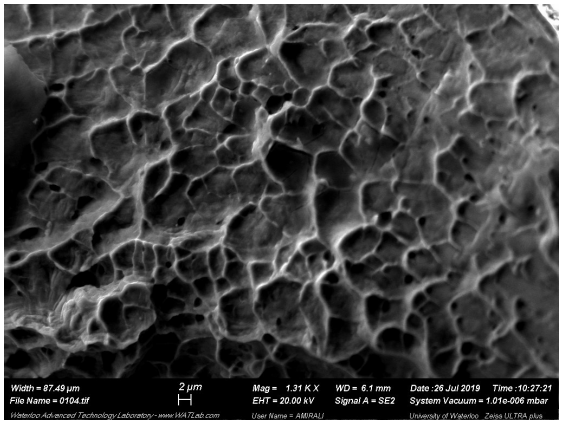
Width = 87.49 µm
File Name = 0104.tif
2 µm
Mag = 1.31 K X
EHT = 20.00 kV
WD = 6.1 mm
Signal A = SE2
Date :26 Jul 2019
System Vacuum = 1.01e-006 mbar
Time :10:27:21
Waterloo Advanced Technology Laboratory - www.WATLab.com
User Name = AMIRALI
University of Waterloo Zeiss ULTRA plus

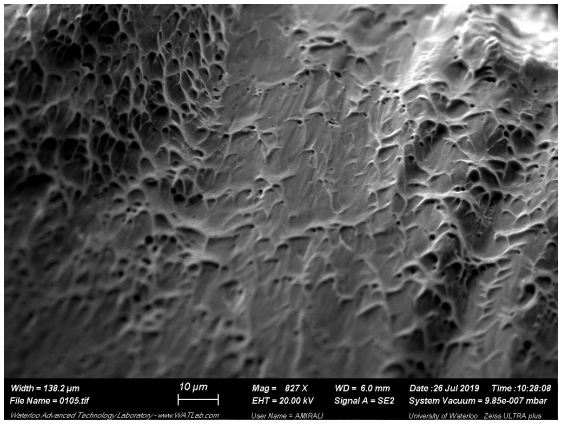
Width = 138.2 µm
File Name = 0105.tif
10 µm
Mag = 827 X
EHT = 20.00 kV
WD = 6.0 mm
Signal A = SE2
Date :26 Jul 2019
System Vacuum = 9.85e-007 mbar
Time :10:28:08
Waterloo Advanced Technology Laboratory - www.WATLab.com
User Name = AMIRALI
University of Waterloo Zeiss ULTRA plus

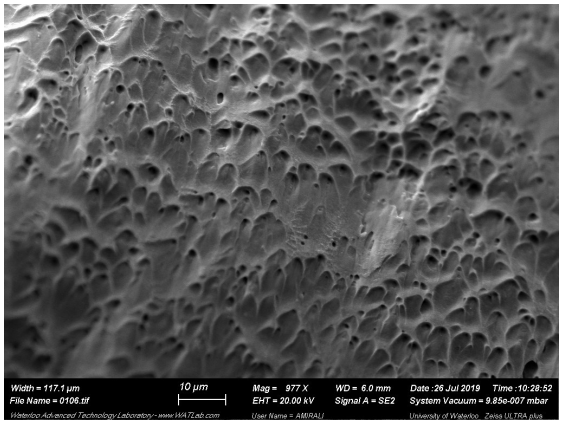
Width = 117.1 µm
File Name = 0106.tif
10 µm
Mag = 977 X
EHT = 20.00 kV
WD = 6.0 mm
Signal A = SE2
Date :26 Jul 2019
System Vacuum = 9.85e-007 mbar
Time :10:28:52
Waterloo Advanced Technology Laboratory - www.WATLab.com
User Name = AMIRALI
University of Waterloo Zeiss ULTRA plus

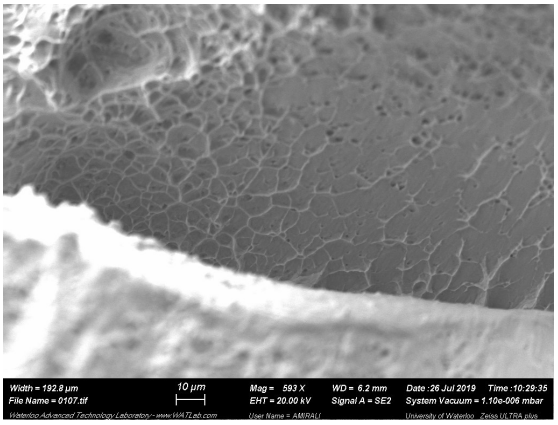
Width = 192.8 µm
File Name = 0107.tif
10 µm
Mag = 593 X
EHT = 20.00 kV
WD = 6.2 mm
Signal A = SE2
Date :26 Jul 2019
System Vacuum = 1.10e-006 mbar
Time :10:29:35
Waterloo Advanced Technology Laboratory - www.WATLab.com
User Name = AMIRALI
University of Waterloo Zeiss ULTRA plus